Triaxiality and the nature of low-energy excitations in ⁷⁶Ge

A. D. Ayangeakaa , 1,2,3,* R. V. F. Janssens, 1,2,† S. Zhu, 4,‡ J. M. Allmond, B. A. Brown, 6,7 C. Y. Wu, M. Albers, 9,8 K. Auranen, B. Bucher, R. M. P. Carpenter, P. Chowdhury, D. Cline, H. L. Crawford, P. Fallon, A. M. Forney, A. Gade, A. D. J. Hartley, A. B. Hayes, I. J. Henderson, F. G. Kondev, Krishichayan, I. Lauritsen, J. Li, D. Little, A. O. Macchiavelli, L. D. Rhodes, A. D. Seweryniak, S. M. Stolze, W. B. Walters, and J. Wu⁹, ** ¹Department of Physics and Astronomy, University of North Carolina at Chapel Hill, Chapel Hill, North Carolina 27599, USA ²Triangle Universities Nuclear Laboratory, Duke University, Durham, North Carolina 27708, USA ³Department of Physics, United States Naval Academy, Annapolis, Maryland 21402, USA ⁴National Nuclear Data Center, Brookhaven National Laboratory, Upton, New York 11973-5000, USA ⁵Physics Division, Oak Ridge National Laboratory, Oak Ridge, Tennessee 37831, USA ⁶Facility for Rare Isotope Beams, Michigan State University, East Lansing, Michigan 48824, USA ⁷Department of Physics and Astronomy, Michigan State University, East Lansing, Michigan 48824, USA ⁸Lawrence Livermore National Laboratory, Livermore, California 94550, USA ⁹Physics Division, Argonne National Laboratory, Argonne, Illinois 60439, USA ¹⁰Department of Physics and Applied Physics, University of Massachusetts Lowell, Lowell, Massachusetts 01854, USA ¹¹Department of Physics and Astronomy, University of Rochester, Rochester, New York 14627, USA ¹²Nuclear Science Division, Lawrence Berkeley National Laboratory, Berkeley, California 94720, USA ¹³Department of Chemistry and Biochemistry, University of Maryland, College Park, Maryland 20742, USA ¹⁴Department of Physics, Duke University, Durham, North Carolina 27708, USA

(Received 27 January 2023; accepted 3 April 2023; published 19 April 2023)

The deformation properties of the low-lying states in ⁷⁶Ge have been investigated following a safe-energy Coulomb excitation measurement with the GRETINA tracking array and CHICO2 heavy-ion counter at the ATLAS accelerator facility at Argonne National Laboratory. A comprehensive set of transition and static *E*2 matrix elements were extracted from the measured differential Coulomb cross sections and compared with results of configuration-interaction shell-model calculations and computations carried out within the framework of the generalized triaxial rotor model. The remarkable agreement between the calculated and experimental data supports a near-maximum triaxial deformation for the ground state of ⁷⁶Ge. In addition, the degree of softness of the asymmetry in ⁷⁶Ge and ⁷⁶Se was investigated using rotational invariants generated from configuration-interaction shell-model wave functions computed with the jj44b and JUN45 effective interactions. The resulting invariants are shown to be consistent with a stiff triaxial deformation in ⁷⁶Ge and a predominantly soft triaxial potential for ⁷⁶Se, in agreement with the conclusions of recent works by this collaboration.

DOI: 10.1103/PhysRevC.107.044314

I. INTRODUCTION

Over the last few years, there has been a notable increase in the number of experimental and theoretical studies dedicated to understanding the nature of low-spin intrinsic excitations in stable and neutron-rich even-even Ge isotopes. While many of these investigations were motivated by the fact that these isotopes have so far eluded satisfactory model descriptions, the vast majority are due to the emergence of ⁷⁶Ge as a candidate nucleus for the hypothetical neutrinoless double beta $(0\nu\beta\beta)$ decay process. The latter follows from the fact that the observation of this lepton number violating process would not only establish the neutrino as a self-conjugate particle, but would also provide a pathway toward the determination of its effective mass, once the nuclear matrix elements (NME) governing the decay are reliably known. These NMEs are not experimental observables and, thus, can only be determined theoretically. Although significant discrepancies between the NME values calculated by different methods remain, efforts to understand and minimize these differences have progressed remarkably in the past few years. Among the many nuclear structure effects studied, deformation due to quadrupole correlations and, thus, the nuclear shape parameters are shown to have a significant impact on the magnitude of the calculated

^{*}ayangeak@unc.edu

[†]rvfj@email.unc.edu

[‡]Deceased.

[§]Present Address: Ernst & Young GmbH, Mergenthalerallee 3-5, D-65760 Eschborn, Germany.

^{||}Present Address: Idaho National Laboratory, Idaho Falls, Idaho 83415, USA.

[¶]Present address: Physics Division, Oak Ridge National Laboratory, Oak Ridge, Tennessee 37831, USA.

^{*}Present address: TRIUMF, 4004 Wesbrook Mall, Vancouver, BC, Canada V6T 2A3.

^{**}Present Address: National Nuclear Data Center, Brookhaven National Laboratory, Upton, New York 11973-5000, USA.

NMEs. Specifically, these NMEs are shown to adopt substantially lower values when the parent and daughter nuclei assume different shapes [1–4], but they are enhanced when similar deformations are involved [4,5]. In addition, it was demonstrated that the calculated NMEs are maximized when spherical symmetry is assumed in both parent and daughter nuclei [6]. These findings, along with effects due to pairing correlations [7], imply that a proper characterization of the ground-state properties and, in particular, an understanding of the role of deformation and axial asymmetry in parent-daughter pairs is critical for reliably calculating the $0\nu\beta\beta$ NMEs.

With only four valence proton particles with respect to the Z = 28 shell closure, the Ge isotopes display a remarkable complexity in their ground-state wave functions and exhibit notable spectral variations with increasing neutron excess. Close to stability, the structure is dominated by phenomena associated with shape transition and coexistence between weakly- and/or strongly deformed structures with varying degrees of shape asymmetry [8], as well as structures impacted by mixing with intruder configurations. As such, these nuclei have provided a challenging testing ground for nuclear models. Indeed, the Ge isotopes have been the subject of extensive investigations using various theoretical formalisms including the Monte Carlo shell model (MCSM) [9], projected shellmodel approaches [10] and shell-model calculations with newly developed effective interactions [11–13]. Mean-field calculations using the five-dimensional collective Hamiltonian (5DCH) based on the Hartree-Fock-Bogoliubov (HFB) model with the Gogny interaction [14], and other selfconsistent approximations employing Skyrme and relativistic interactions [15] are available as well. Calculations within the framework of the interacting boson model (IBM) and its associated variants [16,17] as well as covariant density functionals [18,19] have also been performed. While some of these calculations have been somewhat successful, albeit only qualitatively, in elucidating some of the low-spin properties of these isotopes, many of the salient features, such as the parabolic variation of the energy of the first-excited 0⁺ state along the isotopic chain, have either remained unaccounted for or poorly reproduced. For instance, the calculations of Ref. [19] compute the excitation of this level in ⁷²Ge to be at an energy of about 1.5 MeV above the experimental value and suggest it to be the bandhead of a highly collective structure that has not been observed experimentally. Other systematic investigations of the structure of the even-even Ge nuclei, carried out within the frameworks of the multiquasiparticle triaxial projected shell model (TPSM) [20,21], Gogny-Hartree-Fock-Bogoliubov (HFB) theory, and the Skyrme Hartree-Fock plus pairing in the BCS approximation [22] have, in addition, demonstrated the importance of triaxial collectivity and configuration mixing in reproducing the experimental data.

Triaxiality is an essential feature and plays an important role in determining the structure of Ge isotopes. For example, the unusual level structure of 72 Ge has recently been reinterpreted as being the result of coexistence, with maximum mixing, of two triaxially deformed configurations, based on evidence derived from the rotational-invariant sum-rule analysis of E2 matrix elements associated with the 0_1^+ ground

state and the first-excited 0_2^+ level [23]. Moreover, while triaxiality at low spin is often associated with pronounced γ softness, i.e., with a broad minimum in the (β, γ) deformation plane, a spectroscopic analysis of the levels of the γ - and ground-state bands of ⁷⁴Ge, as presented in Ref. [19], reveals a characteristic transition from a soft to a rigid triaxial structure. In the same way, empirical evidence for rigid-triaxial deformation was proposed, based on the energy pattern of the low-spin structure of ⁷⁶Ge [24], where the phase of the odd-even staggering in the γ band was shown to be consistent with predictions of the phenomenological γ -rigid model [25]. Likewise, the energy staggering of the unusual sequence with suppressed $\Delta I = 2$ crossover transitions recently observed in ⁷⁸Ge [26] displays the phase expected for a γ -rigid structure. It is important to note, however, that while evidence for rigid-triaxial deformation is now well established at high spins, the question of whether such structures exist near the ground state is still a matter of debate and, indeed, represents a fundamental challenge in nuclear structure.

Recently, we reported on a model-independent study of the nature of low-spin triaxial deformation in ⁷⁶Ge following a high-statistics Coulomb excitation measurement performed at the ATLAS facility at Argonne National Laboratory. In this study, shape parameters deduced on the basis of a rotationalinvariant sum-rule analysis provided considerable insight into the underlying collectivity of the ground-state and γ bands. In particular, both sequences were found to be characterized by similar values of the quadrupole (β) and asymmetry (γ) deformation parameters. In addition, compelling evidence for low-spin, rigid triaxial deformation was deduced, based on analysis of the statistical fluctuations of the rotationalinvariant quadrupole asymmetry derived from the measured E2 matrix elements. These results, along with a subset of the deduced matrix elements, were first reported in Ref. [27]. In the present follow-up publication, a more in-depth description of the experimental and data analysis procedures is presented and the complete set of E2 matrix elements extracted from the data is provided. Additionally, the data are compared with results of configuration-interaction (CI) shell-model calculations, originally reported in Ref. [28], and computations carried out within the framework of the triaxial rotor model with independent inertia and electric-quadrupole tensors [29]. Excellent agreement between the experimental and calculated electric-quadrupole properties is observed. In particular, the rotational-invariant shape parameters deduced from the shellmodel calculations agree with the rigid triaxial interpretation of the ⁷⁶Ge low-spin structure.

This article is organized as follows. Section II provides further details about the experiment, while Sec. III presents a methodological description of the process for extracting matrix elements from the Coulomb excitation yields before providing the results. An in-depth discussion of the experimental results along with comparisons with shell-model and triaxial rotor calculations is presented in Sec. IV. Finally, the conclusions are summarized in Sec. V.

II. EXPERIMENTAL DETAILS

The low-lying states of ⁷⁶Ge were populated via multistep Coulomb excitation in two separate experiments performed

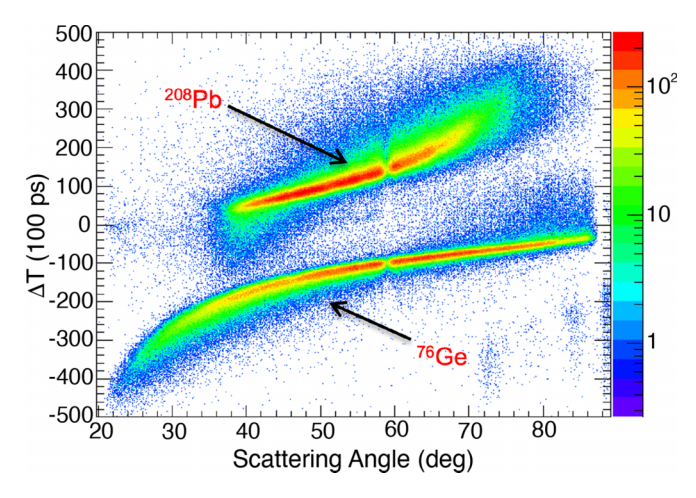


FIG. 1. Differences in the time-of-flight between the projectile and target recoils as a function of scattering angle measured with the CHICO2 detector. A clear separation between the ⁷⁶Ge and ²⁰⁸Pb ions is observed.

at the ATLAS accelerator facility at Argonne National Laboratory. In both measurements, ⁷⁶Ge ions bombarded an enriched 0.5-mg/cm²-thick ²⁰⁸Pb target, sandwiched between a 6 μ g/cm² Al front layer and a 40 μ g/cm² C backing. The γ rays emitted in the deexcitation were detected by the advanced tracking array, GRETINA [30], in kinematic coincidence with scattered reaction products recorded with CHICO2, a twodimensional, pixelated parallel-plate avalanche counter [31]. As a large solid-angle position-sensitive charged-particle array, CHICO2 maintains a mass resolution $(\Delta m/m)$ of $\approx 5\%$ and covers laboratory scattering angles between 20° and 85° in the downstream sector and 96° and 164° upstream, with 1.55° and 2.47° localization in θ (polar angle) and ϕ (azimuthal angle), respectively. In addition, the detector achieves a time resolution of \approx 1.2 ns (FWHM), which is sufficient for measuring the time-of-flight differences $\Delta T_{\rm tof}$ between the reaction products as a function of the polar scattering angle, θ . A two-dimensional histogram depicting ΔT_{tof} as a function of laboratory scattering angle demonstrates a clear separation between the reaction participants, as seen in Fig. 1. The first experiment utilized a subbarrier beam energy of 304 MeV. At the time of this experiment, the GRETINA array consisted of 28 highly segmented coaxial high-purity germanium (HPGe) crystals grouped into seven modules. For the second, two beam energies of 291 and 317 MeV were employed. The 291-MeV energy was chosen to satisfy the "safe energy" criterion [32], which ensures a purely electromagnetic interaction, while the other two were selected to enhance the population of high-spin states in the ground-state and γ bands. For the second measurement, GRETINA comprised 44 crystals, grouped into 11 modules. In both experiments, the time and angular resolution provided by the CHICO2 detector as well as the position information in GRETINA, enabled the event-by-event reconstruction of the reaction kinematics and the precise Doppler correction of the in-flight γ -ray energies. A representative Doppler-reconstructed spectrum, measured in coincidence with the scattered ⁷⁶Ge recoils, is presented in Fig. 2. In all, a total of 21γ rays, linking 17 low-lying states in 76 Ge, were measured. Two additional γ rays (1497 and 2170 keV) were observed, but not included in the analysis, since either they have not been observed in earlier works or their placement in the level scheme is uncertain. These are marked with an asterisk symbol in Fig. 2. The 1410-keV γ ray marked with the # symbol was also excluded in the analysis, as it is most likely a sum peak arising from the simultaneous detection of the 563- $(2_1^+ \rightarrow 0_1^+)$ and 847-keV $(4_1^+ \rightarrow 2_1^+)$ transitions. A partial level scheme incorporating every transition observed in the present measurement is provided in Fig. 3. The seven transitions highlighted in red are those observed by Toh et al. [33] in the most recent ⁷⁶Ge Coulomb excitation measurement prior to the present work. By contrast, transitions in black refer to γ rays observed in Coulomb excitation for the first time, herewith illustrating the resolving power and efficiency of the present experiment. Except for the 2767-keV level, which was reassigned in Ref. [28], the spins and parities of all other levels in Fig. 3 were adopted from earlier decay experiments [34,35], transfer [36], and/or fusion-evaporation [37] reactions.

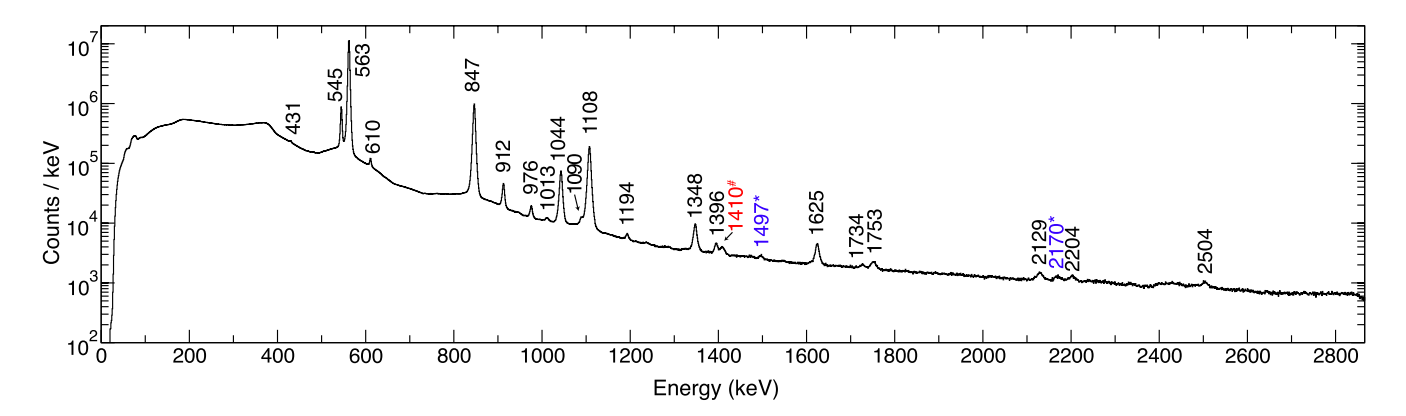


FIG. 2. Doppler-corrected γ -ray spectrum measured with GRETINA following Coulomb excitation of the 76 Ge beam impinging on the 208 Pb target. Peaks labeled in blue and marked with an asterisk correspond to transitions whose placement in the level scheme is unknown. The 1410-keV γ ray is the sum peak arising from the simultaneous detection of the $2_1^+ \rightarrow 0_1^+$, 563- and 847-keV, $4_1^+ \rightarrow 2_1^+$ transitions. These three peaks were not included in the χ^2 minimization (see text for more details).

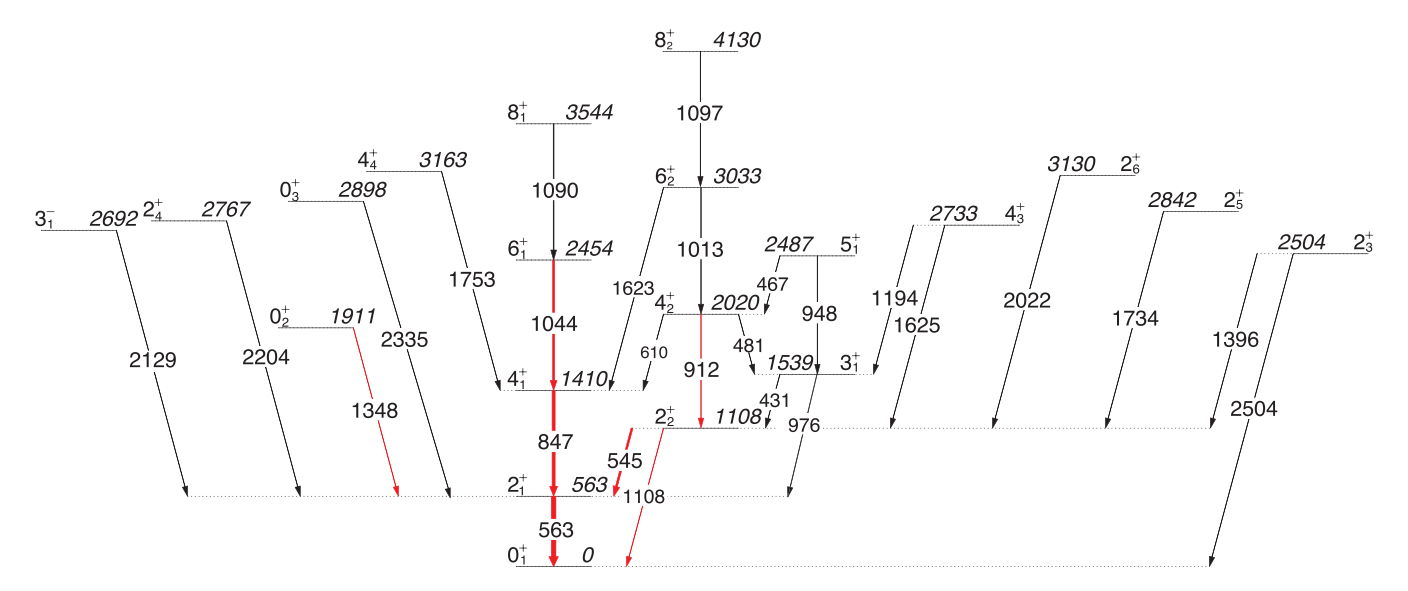


FIG. 3. Partial level scheme of 76 Ge with all the transitions observed in the present Coulomb excitation measurement; red-colored transitions are those observed in Ref. [33], the most recent Coulomb excitation measurement prior to the present work. Transitions in black refer to γ rays observed for the first time in Coulomb excitation. The subscripts on the spin quantum numbers refer to the sequence in which levels of the same spin and parity are observed in this work.

III. DATA ANALYSIS AND RESULTS

The population of nuclear states by multistep Coulomb excitation and their subsequent decay is governed by the reduced matrix elements linking the nuclear states involved. To measure these matrix elements, γ -ray yields derived from the data were analyzed with the semiclassical, least-squares search code, GOSIA [38,39]. This code uses a standard χ^2 function constructed from the measured γ -ray yields and theoretical ones calculated from an initial set of both transition and static matrix elements. Since the excitation probability also depends on the relative phases as well as on the sign and magnitude of the E2 matrix elements, the initial set of these quantities used as starting values in the two-dimensional χ^2 search were chosen to sample all possible signs of the interference term [40].

To enhance the sensitivity to the matrix elements and exploit the dependence of the excitation probability on the particle scattering angle, the data from each of the three beam energies were partitioned into seven angular subsets, corresponding to scattering ranges of 30° – 40° , 40° – 50° , 50° – 60° ,

 $60^{\circ}-70^{\circ}$, $70^{\circ}-85^{\circ}$, $96^{\circ}-130^{\circ}$, and $130^{\circ}-165^{\circ}$. This resulted in a total of about 118 efficiency-corrected γ -ray intensities from 21 data sets corresponding to the different projectile energies and scattering angles. Representative spectra depicting the angular dependence, shown in Fig. 4, indicate that, as the average center-of-mass scattering angle is increased from $\approx 35^{\circ}$ [Fig. 4(a)] to $\approx 147.5^{\circ}$ [Fig. 4(e)], the impact parameter and the distance of closest approach are decreased. As a result, the excitation probability for higher-energy and higher-angular-momentum states via multistep excitation is strongly enhanced at larger scattering angles. As can be seen in the differential population of individual transitions, this enhancement is not only dependent on the scattering angle, but also differs significantly for the various transitions, thereby illustrating the sensitivity of the present data to the individual matrix elements. For the present study, data obtained at the three bombarding energies were analyzed independently, but were later combined as well to check for consistency.

In addition, known spectroscopic data such as lifetimes, branching and E2/M1 mixing ratios were included as constraints of the relevant parameters during the fitting procedure.

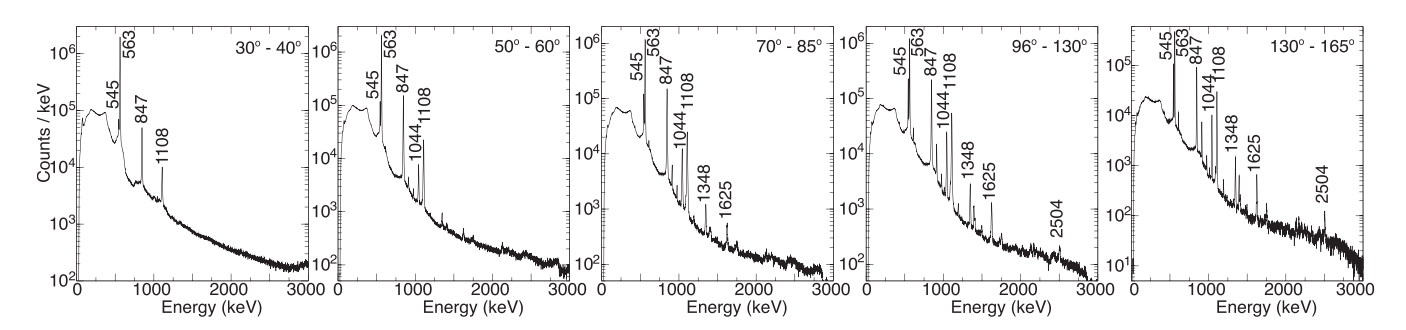


FIG. 4. Spectra after Coulomb excitation of 76 Ge on 208 Pb for five subsets of data corresponding to different ranges of particle-scattering angles. The observation at backward angles of many more γ rays associated with transitions between higher-spin states can be noticed.

TABLE I. Lifetimes (τ) and mixing ratios (δ) used to constrain the minimization process. Data marked with (*) were taken from Ref. [41]. All others were taken from Ref. [28]. The uncertainties are symmetrized for use in GOSIA.

State	Lifetime (ps)	$I_i^\pi o I_f^\pi$	Mixing Ratio (δ)
${2_{1}^{+}}$	26.26(29)*	$2_2^+ \to 2_1^+$	2.5(2)
2_{2}^{+}	11.54(22)*	$3_1^+ \to 2_1^+$	$2.5(2)^{a}$
4_1^+	2.60(59)*	$3_1^+ \to 2_2^+$	1.87(17)
0_{2}^{+}	1.8(9)	$4_2^+ \rightarrow 4_1^+$	0.59(14)
4_{2}^{+}	2.1(15)	$4_2^+ \to 3_1^+$	0.48(9)
6+	0.38(42)	$2_3^+ o 2_2^+$	1.9(2)
5 ₁ ⁺	1.5(8)	$2_3^+ \rightarrow 3_1^+$	0.57(14)
3_	0.231(20)	$4_3^+ \rightarrow 3_1^+$	0.36(6)
4+	0.54(10)	$2_4^+ \rightarrow 2_1^+$	-0.09(2)

^aTaken from Ref. [24].

This information is summarized in Tables I and II. As the excitation process is also influenced by internal conversion at low transition energies and effects associated with the detection system, the γ -ray yields calculated by GOSIA from the input matrix elements were corrected for possible conversions, the finite size and relative efficiency of the γ -ray detectors, as well as for the attenuation of the particle- γ correlation due to deorientation effects during recoil in vacuum. For the present analysis, the BrIcc database [42] was used to compute the internal-conversion coefficients for all observed transitions.

The final set of matrix elements, which best reproduces the experimental γ -ray yields and known spectroscopic data, are displayed in Table III. Convergence was achieved with a minimum χ^2 , normalized to the number of experimental data points, of 0.98 for all three beam energies combined. Overall, a total of 81 E1, E2, E3, and M1 reduced matrix elements were determined. These results are in satisfactory agreement with previous Coulomb excitation measurements [33,43,44]. For all matrix elements, the quoted uncertainties were derived in the standard way by constructing a probability distribution in the space of fitted parameters and requesting

TABLE II. Branching ratios (BR) in the literature for selected transitions used in constraining the χ^2 minimization. Data are taken from Ref. [28]. The uncertainties are symmetrized for use in GOSIA.

$I(I_i^{\pi} \to I_{f1}^{\pi})$	$I(I_i^{\pi} o I_{f2}^{\pi})$	$\mathrm{BR}\bigg[\frac{I(I_i^{\pi} \to I_{f1}^{\pi})}{I(I_i^{\pi} \to I_{f2}^{\pi})}\bigg]$
$2_2^+ \to 0_1^+$	$2_2^+ \to 2_1^+$	0.68(4)
$3_1^+ \to 2_2^+$	$3_1^+ \to 2_1^+$	0.72(7)
$4_2^+ \to 4_1^+$	$4_2^+ \rightarrow 2_2^+$	0.67(3)
$4_2^+ \to 3_1^+$	$4_2^+ \rightarrow 2_2^+$	0.142(15)
$5_1^+ \rightarrow 4_2^+$	$5_1^+ \rightarrow 3_1^+$	0.11(1)
$2_3^+ \to 0_1^+$	$2_3^+ \rightarrow 2_2^+$	0.35(3)
$2_3^+ \to 3_1^+$	$2_3^+ \rightarrow 2_2^+$	0.16(2)
$3_1^- \rightarrow 4_1^+$	$3_1^- \rightarrow 2_1^+$	0.13(2)

the total probability to be equal to the chosen confidence limit (in this case 68.3%). These uncertainties include the statistical and systematic contributions as well as those arising from cross-correlation effects.

IV. DISCUSSION

The transition matrix elements resulting from the present analysis agree, within errors, with those derived from previous Coulomb excitation measurements [33,43–45], albeit with better precision. The only significant exceptions are the magnitudes of the matrix elements associated with decays from the 4_2^+ level, as well as that for the $0_2^+ \rightarrow 2_1^+$ transition. For the latter, Toh et al. [33] report a matrix element with a magnitude of |0.08(3)| eb, in contrast with the present value of $0.144^{+0.002}_{-0.003}$ e b. The discrepancy is likely related to the very weak excitation of the 4_2^+ and 0_2^+ levels in their measurement. In terms of the static moments, the measurements similarly agree, although the absolute magnitude of the present value of -0.24(2) eb for the $\langle 2_1^+ || M(E2) || 2_1^+ \rangle$ diagonal matrix element is in better agreement with the -0.25(8) eb moment measured by Lecomte et al. [43] compared with the -0.19(5) e b one determined in Ref. [33]. However, the measured value of $\langle 2_2^+ || M(E2) || 2_2^+ \rangle = 0.26_{-0.03}^{+0.02} e$ b is lower than the 0.37(8) e b value reported by Toh et al. [33]. Moreover, the reduced transition probabilities deduced from the present matrix elements are also in satisfactory agreement with those determined in the inelastic neutron-scattering measurements reported in Ref. [28]. The latter are presented in the rightmost column of Table III. In general, the negative signs of the diagonal matrix elements for the 2_1^+ , 4_1^+ , and 6_1^+ levels in the ground-state band (K=0) are consistent with a prolate deformation when assuming axial symmetry. The modestly collective character of ⁷⁶Ge being reflected by the large and increasing transition matrix elements for the levels in the 2^+_1 - 6^+_1 sequence is supported by the corresponding reduced transition probabilities B(E2) which have values of up to \approx 60 W.u. (see Table III). Similarly, the positive sign as well as the magnitude deduced for the $\langle 2_2^+ || M(E2) || 2_2^+ \rangle$ diagonal matrix element for the 2^+_2 state in the γ band (K=2) aligns with a prolate deformation, in agreement with the observations of Ref. [33]. In addition, the relatively large values determined for the $\langle 2_1^+ || M(E2) || 2_2^+ \rangle$ and $\langle 2_2^+ || M(E2) || 4_2^+ \rangle$ static matrix elements also agree with a moderately collective structure for the quasi- γ band and show, in the case of the former, the increasing role of triaxiality which enables the strong mixing between the I =2 states in the K = 0 and K = 2 bands. This is also reflected in the nonzero value for the $B(E2; 2_2^+ \rightarrow 2_1^+)/B(E2; 2_1^+ \rightarrow 0_1^+)$ ratio, a sensitive measure of triaxiality. It varies from zero in the axially symmetric limit to 10/7 at $\gamma = 30^{\circ}$, and is always less than two, the limit for a harmonic vibrator.

To further investigate the role of triaxiality and provide insight into the nature of the low-lying states, a generalized version of the triaxial rotor model with independent inertia and electric-quadrupole tensors [29,40,46–48] was applied to the newly deduced E2 matrix elements of 76 Ge. As noted in Ref. [29], this version of the rotor model is a departure from the standard use of irrotational flow moments of inertia

TABLE III. Summary of E1, E2, E3, and E3 matrix elements and reduced transition probabilities for E3 deduced in the present work. Units for reduced transition strengths are μ_N^2 , e^2 b, e^2 b², and e^2 b³ for E3 for E3 transitions, respectively. Accordingly, E3, E3, and E3 transitions are listed in units of E3, E3, and E3 transitions, respectively. Accordingly, E3, E3, and E3 transitions are listed in units of E3, E3, and E3 transitions, respectively. Accordingly, E3, and E3 transitions, respectively.

	$\langle I_i M(\lambda L) I_f angle \uparrow$					$B(\lambda L\downarrow;I_i^\pi\to I_f^\pi)$ [W.u.]		
$I_i^\pi o I_f^\pi$	Mult.	This work	Toh et al. [33]	Refs. [43,44]	$B(\lambda L\downarrow;I_i^\pi\to I_f^\pi)$	This Work	Ref. [28]	
$0_1^+ o 2_1^+$	E2	0.526(2)	0.522(4)	0.550(3)	0.0553(4)	28.9(2)	29(1)	
$0_1^+ ightarrow 2_2^+$	E2	0.089(3)	0.069(10)	0.081(14)	0.0016(1)	0.83(6)	0.90(3)	
$0_1^+ o 2_3^+$	E2	0.061(3)			0.00074(7)	0.39(4)	0.05(2)	
$0_1^+ \rightarrow 2_4^+$	E2	0.054(4)			0.00058(9)	0.31(5)	0.33(6)	
$0_1^+ \rightarrow 2_5^+$	E2	$0.010^{+0.009}_{-0.021}$			$0.00002^{+0.00005}_{-0.00002}$	$0.01^{+0.03}_{-0.01}$		
$0_1^+ o 2_6^+$	E2	0.023(6)			0.00011(6)	0.06(3)	0.06(2)	
$2_1^+ \rightarrow 2_1^+$	E2	-0.24(2)	$-0.19(5)^{a}$	$-0.25(8)^{a}$				
$2_1^+ \rightarrow 4_1^+$	E2	0.795(5)	0.71(4)	0.77(4)	0.0702(9)	36.7(5)	38(9)	
$2_1^+ \to 2_2^+$	E2	$0.535^{+0.003}_{-0.007}$	0.54(3)	0.71(7)	$0.0573^{+0.0006}_{-0.0015}$	$29.9_{-0.8}^{+0.3}$	39^{+5}_{-4}	
$2_1^+ \rightarrow 2_2^+$	M1	$0.175^{+0.006}_{-0.008}$			$0.0061^{+0.0004}_{-0.0006}$	$0.0034^{+0.0002}_{-0.0003}$		
$2_1^+ \to 4_2^+$	E2	$-0.220^{+0.005}_{-0.003}$	0.10(2)		0.0054(2)	$2.81^{+0.13}_{-0.08}$		
$2_1^+ \rightarrow 3_1^+$	E2	0.082(5)			0.0010(1)	0.50(6)		
$2_1^+ \rightarrow 3_1^+$	M1	$0.027^{+0.003}_{-0.003}$			$0.00010^{+0.00002}_{-0.00002}$	$0.00006^{+0.00001}_{-0.00001}$		
$2_1^+ \rightarrow 2_3^+$	E2	$-0.126^{+0.006}_{-0.004}$			$0.0032^{+0.0003}_{-0.0002}$	$1.7^{+0.2}_{-0.1}$		
$2_1^+ \rightarrow 2_3^+$	M1	$0.11^{+0.06}_{-0.28}$			$0.0024^{+0.0034}_{-0.0024}$	$0.0013^{+0.0019}_{-0.0013}$		
$2_1^+ \rightarrow 0_2^+$	E2	0.085(2)	0.08(5)		0.0072(3)	$3.8^{+0.1}_{-0.2}$	5(2)	
$2_1^+ \rightarrow 4_3^+$	E2	$-0.064^{+0.006}_{-0.007}$			$0.00045^{+0.00008}_{-0.00010}$	$0.24_{-0.05}^{+0.04}$		
$2_1^+ \rightarrow 2_4^+$	E2	$0.022^{+0.008}_{-0.005}$			$0.00009^{+0.00007}_{-0.00004}$	$0.05_{-0.02}^{+0.03}$	$0.28(3)$ or 35^{+9}_{-7}	
$2_1^+ \rightarrow 2_4^+$	M1	$0.2^{+0.1}_{-0.4}$			$0.008^{+0.010}_{-0.008}$	$0.005^{+0.006}_{-0.005}$,	
$2_1^+ \rightarrow 2_5^+$	E2	$0.016^{+0.011}_{-0.021}$			$0.00005^{+0.00010}_{-0.00005}$	$0.027^{+0.050}_{-0.027}$	0.32(3)	
$2_1^+ \rightarrow 2_6^+$	E2	$-0.048^{+0.002}_{-0.007}$			$0.00045^{+0.00004}_{-0.00014}$	$0.24_{-0.07}^{+0.02}$		
$2_1^+ \rightarrow 2_6^+$	M1	$1.08^{+0.16}_{-0.06}$			$0.23^{+0.07}_{-0.03}$	$0.13^{+0.04}_{-0.01}$		
$2_1^+ \rightarrow 3_1^-$	<i>E</i> 1	$0.026^{+0.001}_{-0.001}$			$0.000100^{+0.000008}_{-0.000007}$	$0.0086^{+0.0007}_{-0.0006}$		
$2_1^+ \rightarrow 0_3^+$	E2	$0.002^{+0.003}_{-0.005}$			$0.000004^{+0.000021}_{-0.000004}$	$0.002^{+0.011}_{-0.002}$		
$2_1^+ \to 4_4^+$	E2	$0.47^{+0.07}_{-0.02}$			$0.025^{+0.007}_{-0.002}$	$12.8^{+3.8}_{-1.0}$		
$4_1^+ \rightarrow 4_1^+$	E2	$-0.26^{+0.01}_{-0.07}$			0.002	12.0=1.0		
$4_1^+ \rightarrow 6_1^+$	E2	$1.11^{+0.03}_{-0.02}$	0.87(2)		$0.095^{+0.005}_{-0.003}$	50^{+3}_{-2}	91^{+55}_{-48}	
$4_1^+ \rightarrow 4_2^+$	E2	0.61(1)	-0.10(3)		0.041(1)	21.6(7)	7^{+4}_{-3} or 23(13)	
$4_1^+ \rightarrow 4_2^+$	M1	$0.447^{+0.009}_{-0.009}$	0.10(3)		$0.0222^{+0.0009}_{-0.0009}$	$0.0124^{+0.0005}_{-0.0005}$	7_3 01 23(13)	
$4_1^+ \rightarrow 6_2^+$	E2	$-0.186^{+0.030}_{-0.005}$			$0.0027^{+0.0009}_{-0.0001}$	$1.39^{+0.45}_{-0.08}$		
$4_1^+ \rightarrow 3_1^+$	E2	$-0.44^{+0.08}_{-0.05}$			$0.028^{+0.010}_{-0.006}$	$1.55_{-0.08}^{+0.08}$ 15_{-3}^{+5}		
$4_1^+ \rightarrow 5_1^+ $	E2	$-0.08^{+0.09}_{-0.05}$			$0.020_{-0.006}^{+0.0021}$	$0.3^{+1.1}_{-0.3}$		
$4_1^+ \rightarrow 4_3^+$	E2	$0.04^{+0.02}_{-0.03}$			$0.0000_{-0.0006}^{+0.0002}$	$0.09^{+0.12}_{-0.09}$	0.00001(1) or 0.78(40)	
$4_1 \rightarrow 4_3$ $4_1^+ \rightarrow 4_3^+$	M1	$0.9^{+0.2}_{-0.1}$			$0.09^{+0.04}_{-0.02}$	$0.05_{-0.09}^{+0.02}$ $0.05_{-0.01}^{+0.02}$	0.00001(1) 01 0.78(40)	
$4_1 \rightarrow 4_3$ $4_1^+ \rightarrow 4_4^+$	E2	$0.9_{-0.1}$ $0.21(1)$			$0.09_{-0.02}$ $0.0049(5)$	2.6(3)		
$4_1^+ \rightarrow 4_4^+$ $4_1^+ \rightarrow 4_4^+$	M1	$0.21^{+0.02}_{-0.02}$			` '	$0.0027^{+0.0005}_{-0.0005}$		
$4_1^+ \rightarrow 4_4^+ $ $4_1^+ \rightarrow 3_1^-$	<i>E</i> 1	$0.21_{-0.02}^{+0.002} \\ 0.021_{-0.002}^{+0.002}$			$0.0049^{+0.0009}_{-0.0009} \\ 0.00006^{+0.00001}_{-0.00001}$	$0.0027_{-0.0005} \ 0.0052_{-0.0010}^{+0.0010}$		
$4_1^+ \rightarrow 5_1^+ \\ 6_1^+ \rightarrow 6_1^+$	E 1 E 2	$-0.021_{-0.002}^{+0.09}$ $-0.23_{-0.04}^{+0.09}$			$0.00000_{-0.00001}$	$0.0032_{-0.0010}$		
	E 2 E 2				$0.00^{+0.01}$	18+5		
$6_1^+ \rightarrow 8_1^+$		$1.25^{+0.07}_{-0.10}$			$0.09^{+0.01}_{-0.02}$	48^{+5}_{-8} 50+19		
$6_1^+ \rightarrow 6_2^+$	E2	$1.2^{+0.2}_{-0.1}$	0.27(9)a		$0.11^{+0.04}_{-0.02}$	58^{+19}_{-10}		
$2_2^+ \rightarrow 2_2^+$	E2	$0.26^{+0.02}_{-0.05}$	$0.37(8)^{a}$		0.0000(4)	0.5(2)		
$2_2^+ \rightarrow 4_1^+$	E2	0.09(2)	-0.11(1)		0.0009(4)	0.5(2)		

TABLE III. (Continued.)

		$\langle I_i M(\lambda L) I_f angle \uparrow$				$B(\lambda L\downarrow;I_i^\pi\to I_f^\pi)$ [W.u.]	
$I_i^\pi o I_f^\pi$	Mult.	This work	Toh et al. [33]	Refs. [43,44]	$B(\lambda L\downarrow;I_i^\pi\to I_f^\pi)$	This Work	Ref. [28]
$2_2^+ o 4_2^+$	E2	0.472(6)	0.56(2)		0.0248(6)	13.0(3)	18(8)
$2_2^+ \to 3_1^+$	E2	$0.52^{+0.02}_{-0.04}$			$0.039^{+0.003}_{-0.006}$	20^{+2}_{-3}	
$2_2^+ \to 3_1^+$	M1	$0.10^{+0.01}_{-0.01}$			0.0014(3)	0.0008(2)	
$2_2^+ \rightarrow 2_3^+$	E2	$0.38^{+0.01}_{-0.02}$			$0.028^{+0.002}_{-0.003}$	15^{+1}_{-2}	2(1) or 0.02(1)
$2_2^+ \rightarrow 0_2^+$	E2	$0.236^{+0.031}_{-0.006}$	0.06(2)		$0.056^{+0.015}_{-0.003}$	29^{+8}_{-1}	
$2_2^+ o 4_3^+$	E2	$0.60^{+0.01}_{-0.02}$			0.040(2)	21(1)	5(1)
$2_2^+ \rightarrow 2_4^+$	E2	-0.18(2)			0.007(1)	3.4(7)	
$2_2^+ \rightarrow 2_5^+$	E2	$0.002^{+0.006}_{-0.003}$			$0.0000008^{+0.0000120}_{-0.0000008}$	$0.0004^{+0.0063}_{-0.0004}$	0.00007(1)
$2_2^+ \to 2_6^+$	E2	$0.036^{+0.011}_{-0.007}$			$0.0003^{+0.0002}_{-0.0001}$	$0.14^{+0.08}_{-0.05}$	0.27(4)
$2_2^+ \to 0_3^+$	E2	-0.002(2)			$0.000004^{+0.000012}_{-0.000004}$	$0.0021^{+0.0063}_{-0.0021}$	
$2_2^+ \rightarrow 4_4^+$	E2	$0.25^{+0.02}_{-0.05}$			$0.007^{+0.001}_{-0.003}$	$3.5^{+0.6}_{-1.4}$	
$2_2^+ \rightarrow 3_1^-$	E1	$0.012^{+0.001}_{-0.001}$			$0.000022^{+0.000002}_{-0.000003}$	$0.0019^{+0.0002}_{-0.0003}$	
$4_2^+ \rightarrow 4_2^+$	E2	$-0.24^{+0.08}_{-0.04}$					
$4_2^+ \rightarrow 6_1^+$	E2	$0.35^{+0.05}_{-0.03}$	0.21(4)		$0.0094^{+0.0027}_{-0.0016}$	$4.9^{+1.4}_{-0.9}$	
$4_2^+ \rightarrow 6_2^+$	E2	0.49(3)			0.019(2)	10(1)	
$4_2^+ \rightarrow 5_1^+$	E2	$-0.9^{+0.7}_{-0.2}$			$0.07^{+0.12}_{-0.03}$	39^{+60}_{-17}	37^{+42}_{-16} or 85^{+104}_{-67}
$6_2^+ \rightarrow 6_2^+$	E2	$1.3^{+0.2}_{-0.2}$					
$6_2^+ \rightarrow 8_1^+$	E2	$-0.3^{+0.2}_{-0.3}$			$0.0053^{+0.0094}_{-0.0053}$	$2.8^{+4.9}_{-2.8}$	
$6_2^+ \rightarrow 8_2^+$	E2	$0.5^{+0.4}_{-0.3}$			$0.015^{+0.033}_{-0.012}$	$7.8^{+17.3}_{-6.3}$	
$3_1^+ \rightarrow 3_1^+$	E2	$0.13^{+0.08}_{-0.10}$					
$3_1^+ \rightarrow 5_1^+$	E2	$0.9^{+0.4}_{-0.6}$			$0.07^{+0.08}_{-0.07}$	39^{+42}_{-34}	33^{+12}_{-11}
$3_1^+ \to 2_3^+$	E2	$0.25^{+0.02}_{-0.04}$			$0.013^{+0.002}_{-0.004}$	7^{+1}_{-2}	
$3_1^+ \to 4_2^+$	E2	$0.64^{+0.03}_{-0.07}$			$0.046^{+0.004}_{-0.010}$	24^{+2}_{-5}	12^{+6}_{-5} or 56^{+57}_{-32}
$3_1^+ \rightarrow 4_3^+$	E2	$0.35^{+0.04}_{-0.07}$			$0.013^{+0.004}_{-0.006}$	7^{+2}_{-3}	8^{+4}_{-3} or 1.0(2)
$2_3^+ \rightarrow 2_3^+$	E2	$-0.24^{+0.02}_{-0.16}$					
$2_3^+ \to 0_2^+$	E2	$0.32^{+0.02}_{-0.02}$			0.021(2)	11(1)	
$3_1^- \rightarrow 3_1^-$	E2	$0.1^{+1.8}_{-1.5}$					
$5_1^+ \rightarrow 6_2^+$	E2	$-0.74^{+0.10}_{-0.08}$			$0.042^{+0.011}_{-0.009}$	22^{+6}_{-5}	
$4_3^+ \rightarrow 4_3^+$	E2	$0.5^{+0.1}_{-0.2}$					
$2_4^+ \to 2_4^+$	E2	$-0.12^{+0.03}_{-0.12}$					
$2_6^+ \to 2_6^+$	E2	$-0.2^{+0.3}_{-0.2}$					
$4_4^+ \rightarrow 4_4^+$	E2	$0.8^{+0.2}_{-0.2}$				_	
$0_1^+ \rightarrow 3_1^-$	E3	$0.12^{+0.02}_{-0.04}$			$0.0021^{+0.0007}_{-0.0014}$	6^{+2}_{-4}	
$2_2^+ \rightarrow 2_3^+$	<i>M</i> 1	$0.31^{+0.04}_{-0.03}$			$0.019^{+0.005}_{-0.004}$	$0.011^{+0.003}_{-0.002}$	
$2_2^+ \to 2_4^+$	<i>M</i> 1	$0.51^{+0.10}_{-0.05}$			$0.05^{+0.02}_{-0.01}$	$0.03^{+0.01}_{-0.01}$	
$3_1^+ \rightarrow 4_2^+$	M1	0.26(1)			0.0075(6)	0.0042(3)	
$4_2^+ \rightarrow 5_1^+$	M1	$-0.74^{+0.18}_{-0.06}$			$0.050^{+0.024}_{-0.008}$	$0.028^{+0.014}_{-0.005}$	
$3_1^+ \to 2_3^+$	<i>M</i> 1	$0.33^{+0.02}_{-0.03}$			$0.022^{+0.003}_{-0.004}$	$0.012^{+0.001}_{-0.002}$	
$3_1^+ \rightarrow 4_3^+$	<i>M</i> 1	$0.69^{+0.02}_{-0.05}$			$0.053^{+0.003}_{-0.008}$	$0.030^{+0.002}_{-0.004}$	

employed in, for example, the Davydov-Filippov model [25]. Within this generalized triaxial rotor model (GTRM), the E2 matrix elements for states within the ground and γ bands are determined analytically with a minimum set of assumptions [49] and compared with the experimental data. To account for other excited states, such as the 0^+_2 and 2^+_3 levels and their associated matrix elements, a configuration mixing calculation between two triaxial rotors [50] is often considered since these states require and/or imply such mixing. However, due to the almost constant Q^2 and Q^3 values observed for the ground and γ bands (see Ref. [27] for details), a single triaxial rotor based on a simple asymmetric top was determined to

^aCalculated using the published spectroscopic quadrupole moment. ^bThe value of $-0.22^{+0.05}_{-0.03} e$ b previously quoted for this transition in Ref. [27] was in error. The present value of $-0.220^{+0.005}_{-0.003} e$ b is correct.

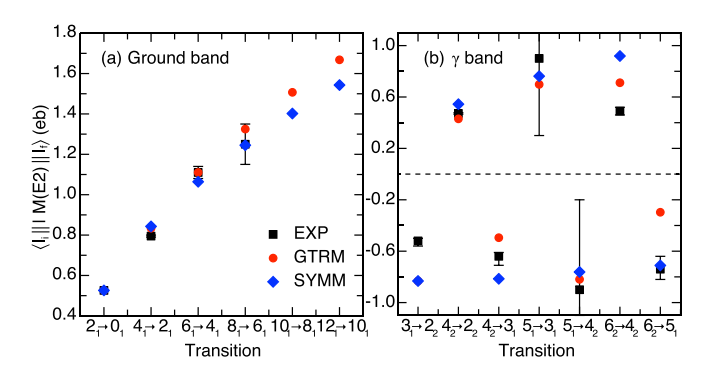


FIG. 5. Experimental transition matrix elements for intraband transitions, $\langle I_i || M(E2) || I_f \rangle$, within the (a) ground-state and (b) γ bands in comparison with theoretical calculations with the generalized triaxial rotor (GTRM) and symmetric rotor models (SYMM). Note that all these states are of positive parity.

be sufficient in describing the primary trend of the E2 matrix elements. The three model parameters required to describe the E2 matrix elements of the triaxial rotor include the intrinsic quadrupole deformation, Q_0 , the asymmetry or triaxiality of the electric-quadrupole tensor, γ , and the asymmetry or mixing angle of the inertia tensor, Γ . In the present study, these parameters were determined analytically from the experimental $\langle 0_1||M(E2)||2_1\rangle$, $\langle 0_1||M(E2)||2_2\rangle$, and $\langle 2_1||M(E2)||2_1\rangle$ matrix elements (cf. Ref. [47]), yielding $Q_0=1.69(1)$ e b, $\gamma=25.4(5)^\circ$, and $\Gamma=-15.8(4)^\circ$.

Figures 5(a) and 5(b) compare results of these calculations, designated as (GTRM), with the experimental transition matrix elements for the yrast and γ bands. For completeness, calculations for a symmetric rotor (SYMM) are also included in Fig. 5. Clearly, both versions of the rotor model reproduce the ground-state [Fig. 5(a)] and γ intraband [Fig. 5(b)] transition matrix elements satisfactorily. This is not unexpected, since both models provide nonzero body projections on the symmetry axis which manifest as K=0 (ground-state) and

 $K = 2 (\gamma)$ sequences with in-band transitions governed primarily by the quadrupole deformation parameter β . Beyond this point, however, the symmetric rotor model fails to account for the data, since it provides no mixing between the two bands. In contrast, the asymmetry in the electric tensor inherent in the GTRM allows transitions between these bands. This is evinced in Fig. 6, where the calculated transition strengths between the ground-state and γ bands are in good agreement with the data. In particular, the model predicts large values when the experimental ones are large as well as when they are small. Overall, the data and calculations follow the same trend. However, there is clear failure in reproducing some of the matrix elements associated with $\Delta I = 0, 1$; $\Delta K = 2$ transitions, which have been shown to be very sensitive to interference effects [47,48]. Except for the 4⁺₂ state, another important outcome is the ability of the GTRM calculations to reproduce the static E2 matrix elements $\langle I_i || M(E2) || I_i \rangle$. This is presented in Fig. 7, where the experimental $\langle I_i || M(E2) || I_i \rangle$ values and their trends with spin are well reproduced by the triaxial rotor model. These results indicate that the triaxial rotor model with independent inertia and electric-quadrupole tensors is able to predict the experimental data with satisfactory accuracy, implying that a departure from axial symmetry is necessary in order to account for the low-spin spectral variations in this nucleus.

The excitation characteristics of low-lying states in 76 Ge were also analyzed by examining the behavior of the three moments of inertia as a function of axial asymmetry, γ . Following the prescription of Ref. [51], the moments were extracted, within the framework of the triaxial rotor model with independent electric-quadrupole and inertia tensors, using the experimental 2_1^+ and 2_2^+ energies and a mixing strength derived from a fit to the measured E2 matrix elements. The resulting moments, \mathcal{J}_1 , \mathcal{J}_2 , and \mathcal{J}_3 , associated with the three principal axes are given as a function of the triaxiality parameter, γ , in Fig. 8. For reference, data for 12 other nuclei with well-delineated γ bands and yrast energy ratios

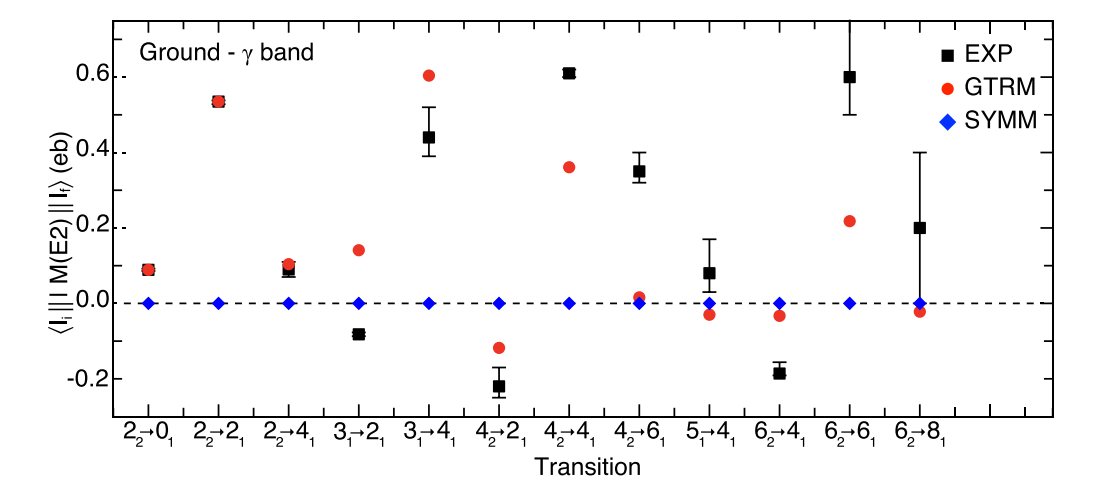


FIG. 6. Experimental transition matrix elements for transitions linking the ground-state and γ bands in comparison with theoretical calculations with the generalized triaxial rotor (GTRM) and symmetric rotor (SYMM) models. The failure of the asymmetric model to reproduce these matrix elements is evident, implying that a departure from axial symmetry is necessary to account for the data on these low-lying transitions.

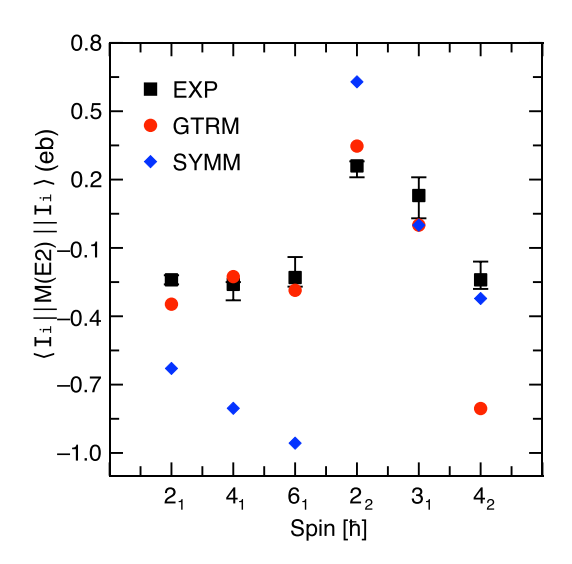


FIG. 7. Comparisons of the static quadrupole moments $\langle I_i||M(E2)||I_i\rangle$ in the ground and quasi- γ bands with the generalized triaxial rotor (GTRM) and symmetric rotor models (SYMM). Note that all these states are of positive parity.

 $R_{4/2}=E(4_1^+)/E(2_1^+)>2.7$, another indicator of triaxiality, are also included in this figure. These are plotted relative to the irrotational moments of inertia, indicated by the solid lines. Similar to the scenario established in 110 Ru [52], the extracted moments for 76 Ge also show a $\mathcal{J}_1>\mathcal{J}_2\sim\mathcal{J}_3$ relation, as expected for a rigid triaxial nucleus with $\gamma\approx30^\circ$. It is important to note, however, that while the GTRM relaxes the irrotational flow requirement, the relative moments of inertia extracted on the basis of independent electric-quadrupole and inertia tensors are qualitatively consistent with irrotational flow. The absolute values, however, are between the irrotational and rigid flow limits.

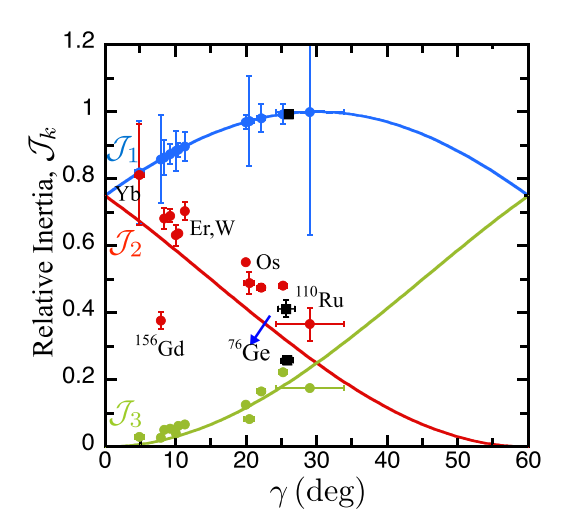


FIG. 8. The relative moments of inertia for all three axes as a function of axial asymmetry, γ . The experimental values (circles) have been normalized to the irrotational values (lines) through the 1 axis. Reproduced from Ref. [51]. Note: the ⁷⁶Ge values are represented by black squares.

As noted above, the experimental matrix elements presented in Table III were used in an earlier publication [27] to investigate the nature of triaxial deformation in ⁷⁶Ge via the rotational-invariant sum-rule technique [53–55]. This method is model independent and enables the determination of the nuclear charge distribution from the expectation values of invariant products of the collective E2 operator via expansion over the experimental reduced E2 matrix elements associated with the states. In particular, it relates the experimentally determined E2 matrix elements with the collective quadrupole deformation defined in the intrinsic frame of the nucleus by constructing a number of collective quadrupole invariants, expressed as functions of the two charge deformation parameters, Q and δ . To first order, the $\langle Q^2 \rangle$ and $\langle \cos 3\delta \rangle$ invariants define the average measure of the magnitude of the symmetric quadrupole deformation and the departure from axial symmetry (triaxiality) of a charged ellipsoid, respectively. These are analogous to the elongation parameter β and the collectivemodel asymmetry angle γ in the Bohr Hamiltonian [56]. The invariant $\langle Q^2 \rangle$ includes both static and dynamic contributions to the symmetry deformation and is related to the root-meansquare of the Bohr variable:

$$\beta_{\rm rms} = \frac{4\pi}{3ZR^2} \sqrt{\langle Q^2 \rangle},\tag{1}$$

where $R=1.2A^{1/3}$ and Z and A are the atomic and mass numbers, respectively. Similarly, the root-mean-square of the quadrupole asymmetry $\langle \cos 3\delta \rangle$ corresponds to the asymmetry angle γ :

$$\delta_{\rm rms} = \frac{1}{3} \arccos\left(\langle \cos 3\delta \rangle\right).$$
 (2)

The asymmetry angle derived in this way provides a good measure of the triaxiality of the nuclear shape for a state but is not sensitive to dynamic shape fluctuations and is, thus, incapable of distinguishing between soft and rigid triaxiality. For the latter purpose, the sum-rule technique allows for higher-order invariants to be constructed, albeit, with a larger set of matrix elements. In particular, the relative stiffness or softness in $\langle Q^2 \rangle$ and $\langle \cos 3\delta \rangle$ can be determined by evaluating their statistical fluctuations, or variance, $\sigma(Q^2)$ and $\sigma(\cos 3\delta)$ over a range of reduced E2 matrix elements. Following this approach, it was demonstrated in Ref. [27] that the E2 properties of ⁷⁶Ge are strongly correlated with the macroscopic quadrupole collective degrees of freedom. In particular, both the ground-state and γ bands were shown to be characterized by the same $\langle Q^2 \rangle$ values, with an average of $\approx 0.30 e^2 b^2$, corresponding to a quadrupole deformation of $\beta_{\rm rms} \approx 0.28$ over the observed spin range. The notable similarity and overall constancy of the $\langle Q^2 \rangle$ values in both sequences confirms the presence of strong correlations between the E2 properties and, hence, the same deformation, as anticipated for collective behavior. Compared with $\langle Q^2 \rangle$, however, the $\langle \cos 3\delta \rangle$ invariant was shown to exhibit a small increase with spin, although a constant value was not ruled out within the quoted uncertainties. The average value of $\langle \cos 3\delta \rangle \approx 0.15$ for the ground-state band corresponds to a deformation δ_{rms} of $\approx 27^{\circ}$, in line with expectations for a welldefined triaxial shape. Within the quoted uncertainties, the $\langle \cos 3\delta \rangle$ behavior for the γ band was similarly constant and

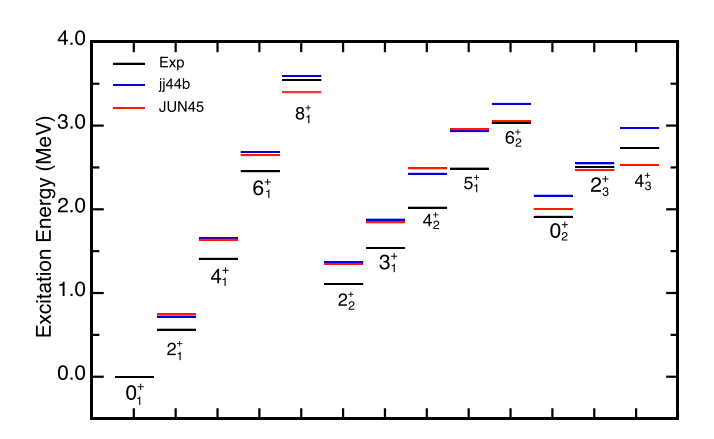


FIG. 9. Comparison of the experimental levels energies with theoretical ones computed with the jj44b and JUN45 interactions (see text for details).

averaged 0.24, corresponding to an asymmetry angle, δ_{rms} , of $\approx\!25^{\circ}$. Hence, the quadrupole asymmetry, as determined from the $\langle\cos3\delta\rangle$ invariant, provides compelling evidence for triaxial deformation in both the ground-state and γ bands, in agreement with the interpretation proposed in Ref. [24], based on the pattern observed for the energy staggering in the latter sequence. These results, along with the analysis of the statistical fluctuations of the invariants, indicate that ⁷⁶Ge is triaxially deformed at low spin with appreciable rigidity in both the β and γ degrees of freedom. For further details on the model-independent analysis summarized here, the interested reader is referred to Ref. [27].

In the present investigation, the comprehensive set of experimental reduced E2 matrix elements and corresponding reduced transition probabilities, B(E2), are compared with results of large-scale shell-model calculations performed with realistic interactions based on a G-matrix renormalized Bonn-C potential. The calculations were carried out in the jj44 model space which comprises a ⁵⁶Ni inert core and the $0f_{7/2}$, $1p_{3/2}$, $1p_{1/2}$, and $0g_{9/2}$ proton and neutron orbitals. The calculations were performed using the shell-model code NUSHELLX [57] with isoscalar effective charges of $e_{\pi} = 1.8e$ and $e_{\nu} = 0.8e$ for both the jj44b [28] and JUN45 [12] Hamiltonians. These Hamiltonians are tuned for the $f_{5/2}pg_{9/2}$ model space and are specifically designed to explore the role of neutron multiparticle-hole excitations from the fp shell into the $g_{9/2}$ orbital. They have been extensively used to predict spectral properties of low-lying states in the $A \approx 60-70$ region with notable accuracy.

A comparison of the experimental level energies with results of the shell-model calculations using the two interactions is displayed in Fig. 9. It includes levels up to 8^+ in the ground-state band and 6^+ in the γ band, as well as the nonyrast 0_2^+ , 2_3^+ , and 4_3^+ levels. Overall, both interactions account for the experimental levels rather well and, except for the 8_1^+ , 2_3^+ , and 4_3^+ levels where the JUN45 interaction underestimates the experimental data, the theoretical predictions appear systematically higher in excitation energy. Quantitatively, the JUN45 interaction agrees with the data somewhat better than the jj44b one. The former reproduces the exper-

TABLE IV. Comparison of experimental reduced transition strengths with those obtained with shell-model calculations using the jj44b and JUN45 effective interactions.

	Ì	$B(E2; I_i \rightarrow I_f)$ W.u.				
$I_i^\pi o I_f^\pi$	Expt.	jj44b	JUN45			
$2_1^+ \to 0_1^+$	28.9(2)	31.8	28.5			
$4_1^+ \rightarrow 2_1^+$	36.7(5)	42.4	38.7			
$6_1^+ \rightarrow 4_1^+$	50^{+3}_{-2}	44.9	41.8			
$8_1^+ \to 6_1^+$	48^{+5}_{-8}	39	39			
$2_2^+ \rightarrow 0_1^+$	0.83(6)	0.03	0.60			
$2_2^+ \to 2_1^+$	$29.9^{+0.3}_{-0.8}$	39.9	43.6			
$4_1^+ \rightarrow 2_2^+$	0.5(2)	0.13	0.01			
$4_2^+ \rightarrow 2_1^+$	$2.81^{+0.13}_{-0.08}$	0.06	0.40			
$4_2^+ \to 2_2^+$	12.9(3)	13.5	9.46			
$4_2^+ \rightarrow 4_1^+$	21.6(7)	10.5	4.41			
$3_1^+ \rightarrow 2_1^+$	0.50(6)	0.03	1.05			
$3_1^+ \to 2_2^+$	20^{+2}_{-3}	56.5	49.3			
$3_1^+ \rightarrow 4_1^+$	15^{+5}_{-3}	24.7	27.6			
$0_2^+ \to 2_1^+$	$3.8^{+0.1}_{-0.2}$	0.23	8.62			
$0_2^+ \to 2_2^+$	29^{+8}_{-1}	0.45	0.35			
$2_3^+ \to 0_1^+$	0.39(4)	0.24	0.74			
$2_3^+ \rightarrow 2_1^+$	$1.7^{+0.3}_{-0.2}$	0.000003	0.24			
$2_3^+ \rightarrow 2_2^+$	15^{+1}_{-2}	0.07	0.73			
$2_3^+ \to 3_1^+$	7^{+1}_{-2}	0.18	0.87			
$6_1^+ \rightarrow 4_2^+$	$4.9_{-0.9}^{+1.4}$	0.02	0.75			

imental data with a root-mean-square deviation of 150 keV compared with 200 keV for the latter. The correspondence between the calculated and experimental energies for the yrast states (up to 6^+) is essentially the same for both interactions, the only exception being JUN45 underestimating the 8_1^+ state by about 147 keV, while jj44b predicts it to be located 64 keV above the experimental value.

Tables IV and V present the calculated reduced transition probabilities, B(E2), as well as the spectroscopic quadrupole moments, Q_s , computed with the two effective interactions. These are compared with the experimental values deduced from the measured matrix elements. On the whole, the calculations provide a sufficiently good reproduction of the

TABLE V. Theoretical spectroscopic quadrupole moments, $Q_s(I)$, in comparison with the experimental values deduced from the measured diagonal matrix elements.

		9	$Q_s(I)$ [e b]			
I^{π}	$\langle I M(E2) I\rangle$	Expt.	jj44b	JUN45		
${2_{1}^{+}}$	-0.24(2)	-0.18(2)	-0.19	+0.030		
2_{2}^{+}	$+0.26^{+0.02}_{-0.05}$	$+0.20^{+0.02}_{-0.04}$	+0.20	-0.007		
4_{1}^{+}	$-0.26^{+0.01}_{-0.07}$	$-0.197^{+0.008}_{-0.053}$	-0.18	-0.008		
4_{2}^{+}	$-0.24^{+0.08}_{-0.04}$	$-0.18^{+0.06}_{-0.03}$	-0.51	-0.59		
61+	$-0.23^{+0.09}_{-0.04}$	$-0.16^{+0.06}_{-0.03}$	-0.15	-0.15		

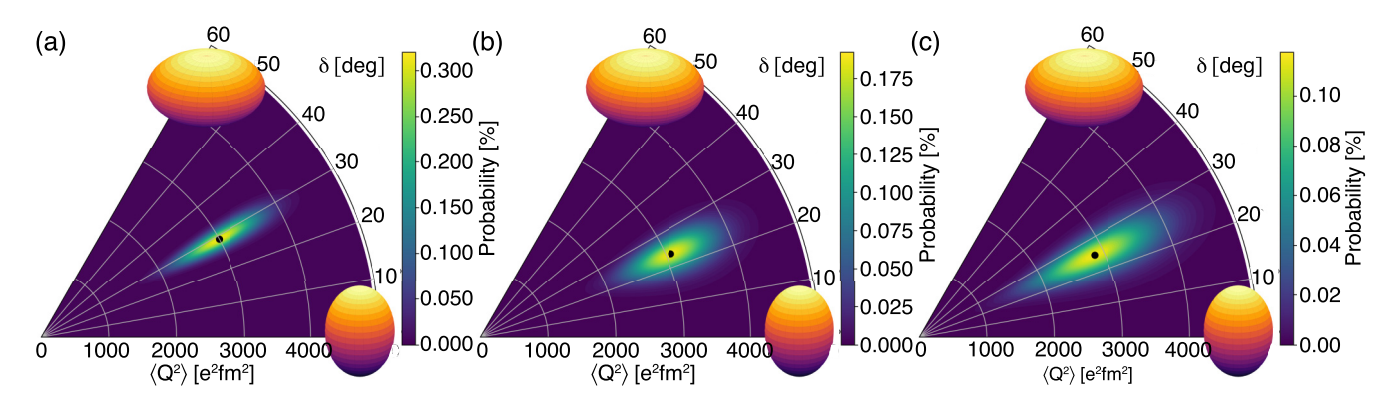


FIG. 10. The absolute quadrupole and asymmetry deformations mapped in the $(\langle Q^2 \rangle, \delta)$ space for the ⁷⁶Ge ground state. (a) The experimental values are shown alongside quadrupole invariants computed with the configuration-interaction shell model using (b) the jj44b and (c) JUN45 effective interactions. Statistical fluctuations describing the measure of the relative stiffness of the deformations are presented as standard deviations of a normal distribution.

measured strengths for both the ground-state and γ -band transitions. In particular, the $2_1^+ \rightarrow 0_1^+$ and $4_1^+ \rightarrow 2_1^+$ strengths are calculated almost exactly by the JUN45 interaction, with the corresponding values predicted by the jj44b calculations being only a few units above the experimental values. Similarly, the measured strengths of 50(2) and 48^{+15}_{-20} W.u. for the $6^+_1 \rightarrow 4^+_1$ and $8_1^+ \rightarrow 6_1^+$ transitions, respectively, are well reproduced by both interactions, although, in this case, the jj44b computation performs slightly better than the JUN45 one. Relative to the 0.98(2) W.u. strength for the $2_2^+ \rightarrow 0_1^+$ transition, the one for the $2^+_2 \rightarrow 2^+_1$ transition is experimentally determined to be quite large and both interactions account for the observation. However, the JUN45 interaction provides a better agreement for the $2^+_2 \rightarrow 0^+_1$ strength, which is underestimated by the jj44b computation. Likewise, the measured strength of 0.39(4) W.u. for the $2_3^+ \rightarrow 0_1^+$ transition is well reproduced by the JUN45 interaction. Thus, except for the $2_3^+ \rightarrow 2_1^+$ strength, which is significantly underestimated by the jj44b computation, the measured strengths are accounted for by the present configuration-interaction computations. These results signify that the choice of effective charges used in these calculations are appropriate for this nucleus, a conclusion that is further reinforced by the remarkable agreement between the measured spectroscopic quadrupole moments and those computed within the ji44b space (Table V). Here, while the JUN45 interaction flips the signs and considerably underestimates the magnitudes of the 2_1^+ and 2_2^+ quadrupole moments, thereby predicting oblate deformation (positive quadrupole moment), the ji44b interaction accurately predicts both the signs and magnitudes (within errors) of the measured moments, consistent with a potential localized within the prolate

The spectroscopic quadrupole moments also inform on the triaxiality of the nuclear shape. For axially asymmetric nuclei, the magnitude of the spectroscopic quadrupole moment determined in the laboratory frame using the diagonal matrix elements Q_s is often a fraction of the intrinsic quadrupole moment derived from the reduced transition matrix elements (under the assumption of an axially symmetric rigid rotor) Q_0 . In the present case, the experimental $Q_s(2_1^+)$ value is

much smaller than the axially symmetric $Q_0(2_1^+)$ moment,¹ as expected for an asymmetrically deformed shape. Similarly, the shell-model-computed absolute ratio $|Q_s/Q_0| = 0.85$ for the 2_1^+ state, determined within the jj44b space, is in satisfactory agreement with the experimentally determined value of 0.86(3). This result further reinforces the validity of these calculations and highlights the role of triaxiality in the ground state. Note that the corresponding ratio determined using the JUN45 interaction is at variance with the experimental data.

To gain further insight into the nature of triaxial deformation in ⁷⁶Ge, the reduced E2 matrix elements computed from the shell-model calculations with the two interactions were used to calculate the two rotational invariants associated with the absolute quadrupole deformation $\langle Q^2 \rangle$ and the degree of asymmetry $\langle \cos 3\delta \rangle$, as well as their respective degrees of softness, $\sigma \langle Q^2 \rangle$ and $\sigma \langle \cos 3\delta \rangle$ for the 0_1^+ ground state. These calculations were performed using a method similar to that presented in Ref. [58]. It should be pointed out that an alternative method of evaluating these quadrupole invariants has recently been presented in Ref. [59]. While this latter method provides an almost exact solution, the results are effectively similar to those derived here. To ensure sufficiently good convergence, E2 transition and diagonal matrix elements linking the 0_1^+ level with the 2^+ states up to the 2_6^+ level were used. A comparison of the resulting invariants with those determined from the experimental matrix elements is displayed in Fig. 10. These are presented in the $(\langle Q^2 \rangle, \delta)$ space, where the statistical fluctuations (that provide a measure of the stiffness of the deformation) are treated as standard deviations within a normal distribution. It can be seen that, although the ii44b calculations [Fig. 10(b)] provide a slightly better quantitative measure of the absolute deformation and a narrower spread in the $\langle O^2 \rangle$ invariant compared with the JUN45 computation [Fig. 10(c)], the two interactions qualitatively reproduce both the absolute magnitudes of the quadrupole deformation (with an effective value of about 0.29 confined within the prolate

¹Calculated using the rotational model expression: $Q_0(2_1^+) = \frac{2}{7}\sqrt{16\pi B(E2; 2_1^+ \to 0_1^+)/5}]^{1/2}$.

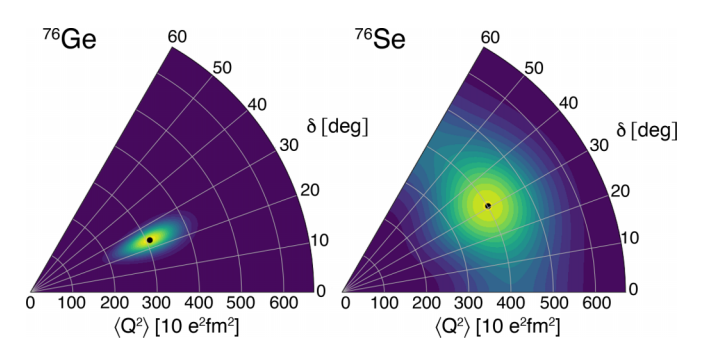


FIG. 11. Configuration-interaction shell-model deformation parameters in the $(\langle Q^2 \rangle, \delta)$ deformation plane computed with the jj44b effective interaction for the ground states of ⁷⁶Ge and ⁷⁶Se. The black dot represent the root-mean-square $\langle Q^2 \rangle$ and δ value in each nucleus

sector) and the degree of asymmetry. For both interactions, the fluctuation in the asymmetry, with an effective value of $\approx\!27^\circ$, is computed with a relatively narrow spread $(\approx\!4^\circ)$. This compares well with the experimentally deduced asymmetry and spread of $\approx\!29^\circ$ and $\approx\!2^\circ$, respectively, and indicates that the ground state of ^{76}Ge is characterized by a sizable, stiff triaxial deformation. The results further suggest that the effective charges and the two interactions employed in the present shell-model calculations are able to reproduce well the underlying structure of ^{76}Ge , and its spectroscopic properties.

Finally, to explore the implications of these results for theoretical efforts aiming to calculate nuclear matrix elements relevant for $0\nu\beta\beta$ decay, the present comparisons were extended to ⁷⁶Se, the daughter in the ⁷⁶Ge double β decay process. Similar to ⁷⁶Ge, the configuration-interaction shell-model calculations for ⁷⁶Se were performed within the same jj44 model space consisting of the $0f_{7/2}$, $1p_{3/2}$, $1p_{1/2}$, and $0g_{9/2}$ orbitals for protons and neutrons using the shell-model code NuShellX with the JUN45 and jj44b Hamiltonians. In these calculations, an isoscalar effective charge of $e_p + e_n = 2.6$ was chosen to reproduce the experimental $B(E2; 2_1^+ \rightarrow 0_1^+)$ value for the jj44b Hamiltonian. More details about these calculations can be found in Ref. [60], where they were originally presented. Figures 11 and 12 provide contour plots in the $(\langle Q^2 \rangle, \delta)$ deformation plane generated from E2 ma-

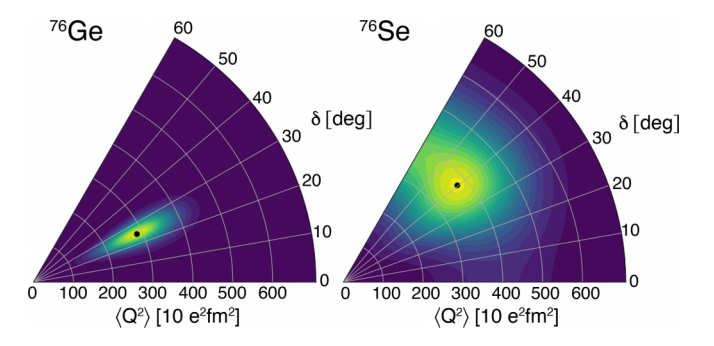


FIG. 12. Configuration-interaction shell-model deformation parameters in the $(\langle Q^2 \rangle, \ \delta)$ deformation plane computed with the JUN45 effective interaction for the ground states of ⁷⁶Ge and ⁷⁶Se. The black dot represent the root-mean-square $\langle Q^2 \rangle$ and δ value in each nucleus.

trix elements determined from the shell-model calculations with the two interactions. These are displayed alongside the configuration-interaction calculations for ⁷⁶Ge. A clear distinction between the ground-state structures of ⁷⁶Ge and ⁷⁶Se is seen in both calculations. While a relatively rigid triaxial configuration is evident for ⁷⁶Ge in the ji44b calculations, the computed ground state of ⁷⁶Se supports a soft triaxial minimum, with a dispersion essentially covering the entire oblate and prolate sectors. In this space, the ground state of ⁷⁶Se is characterized by a larger, but less well-defined effective quadrupole deformation than ⁷⁶Ge, in agreement with experimental observations of triaxiality previously reported in Ref. [61]. A similar conclusion can be drawn from the JUN45 computation, except, here the effective asymmetry of 76 Se (with a dispersion of $\approx 40^{\circ}$ consistent with a soft triaxiality) is distinctively localized within the oblate sector. It is noteworthy that the dispersion values in the asymmetry of ⁷⁸Se for JUN45 and ji44b are roughly in agreement with those computed using the same interactions with the formalism of Ref. [59]. Therefore, these results collectively indicate that the ground states of ⁷⁶Ge and ⁷⁶Se are characterized by sizable quadrupole and asymmetry deformations, albeit with markedly different degrees of triaxial rigidity. Consequently, these observations impact the nuclear matrix elements relevant for $0\nu\beta\beta$ decay: the various theoretical approaches will have to reproduce the parent ⁷⁶Ge as a rigid triaxial rotor while also allowing for soft triaxiality in the ⁷⁶Se daughter.

V. CONCLUSIONS

An extensive study of the deformation characteristics of the low-lying states of ⁷⁶Ge has been undertaken following a multistep Coulomb excitation measurement performed using the y-ray tracking array, GRETINA, and the CHICO2 particle detector. A comprehensive set of reduced E2 transition and static matrix elements was deduced using the semiclassical coupled-channel code GOSIA. These were compared with results of theoretical calculations carried out within the framework of the generalized triaxial rotor model, which provided an accurate reproduction of the experimental matrix elements and, herewith, support the proposed triaxial interpretation. In addition, the low spin and, in particular, the degree of softness of the asymmetry deformation in ⁷⁶Ge and ⁷⁶Se was investigated using the rotational-invariant sum-rule technique with configuration-interaction shell-model wave functions computed with the jj44b and JUN45 effective interactions. The calculated invariants indicate a near-maximal stiff triaxial deformation in ⁷⁶Ge and a predominantly soft triaxial potential for ⁷⁶Se, in agreement with the conclusions of earlier works of Refs. [27,61]. These results are important for calculations aiming to determine the nuclear matrix elements relevant for $0\nu\beta\beta$ decay.

ACKNOWLEDGMENTS

This work was funded by the U.S. Department of Energy, Office of Science, Office of Nuclear Physics, under Grants No. DE-SC0023010 (UNC), No. DE-FG02-97ER41041 (UNC), No. DE-FG02-97ER41033 (TUNL), No. DE-FG02-97ER41041 (UNC), No. DE-FG02-97ER41033 (TUNL), No. DE-FG02-97ER41041 (UNC), NO. DE-FG

08ER41556 (MSU), No. DE-FG02-94ER40848 (UML), and No. DE-FG02-94ER4084 (Maryland), and under Contracts No. DE-AC02-06CH11357 (ANL), No. DE-AC52-07NA27344 (LLNL), No. DE-AC02-05CH11231 (LBNL), No. DE-AC05-00OR22725 (ORNL), and by the National Science Foundation under Grants No. PHY-1565546, No.

PHY-2110365 (MSU), No. DE-SC0020451 (MSU), and No. PHY-1502092 (USNA). GRETINA was funded by the U.S. DOE, Office of Science, Office of Nuclear Physics under the ANL and LBNL contract numbers above. This research used resources of ANL's ATLAS facility, which is a DOE Office of Science User Facility.

- [1] J. Menendez, A. Poves, E. Caurier, and F. Nowacki, Proc. Int. Sch. Phys. Fermi 170, 163 (2009).
- [2] D.-L. Fang, A. Faessler, V. Rodin, and F. Šimkovic, Phys. Rev. C 83, 034320 (2011).
- [3] M. T. Mustonen and J. Engel, Phys. Rev. C 87, 064302 (2013).
- [4] J. M. Yao and J. Engel, Phys. Rev. C 94, 014306 (2016).
- [5] T. R. Rodríguez and G. Martínez-Pinedo, Phys. Rev. Lett. 105, 252503 (2010).
- [6] J. M. Yao, L. S. Song, K. Hagino, P. Ring, and J. Meng, Phys. Rev. C 91, 024316 (2015).
- [7] N. L. Vaquero, T. R. Rodríguez, and J. L. Egido, Phys. Rev. Lett. 111, 142501 (2013).
- [8] P. E. Garrett, M. Zielińska, and E. Clément, Prog. Part. Nucl. Phys. 124, 103931 (2022).
- [9] D. J. Dean, K. Langanke, H. Nam, and W. Nazarewicz, Phys. Rev. Lett. 105, 212504 (2010).
- [10] P. A. Dar, R. Devi, S. K. Khosa, and J. A. Sheikh, Phys. Rev. C 75, 054315 (2007).
- [11] M. Hasegawa, T. Mizusaki, K. Kaneko, and Y. Sun, Nucl. Phys. A 789, 46 (2007).
- [12] M. Honma, T. Otsuka, T. Mizusaki, and M. Hjorth-Jensen, Phys. Rev. C 80, 064323 (2009).
- [13] S. J. Q. Robinson, L. Zamick, and Y. Y. Sharon, Phys. Rev. C 83, 027302 (2011).
- [14] L. Gaudefroy, A. Obertelli, S. Péru, N. Pillet, S. Hilaire, J. P. Delaroche, M. Girod, and J. Libert, Phys. Rev. C 80, 064313 (2009).
- [15] J. Dobaczewski, W. Nazarewicz, J. Skalski, and T. Werner, Phys. Rev. Lett. 60, 2254 (1988).
- [16] J. Elliott, J. Evans, V. Lac, and G. Long, Nucl. Phys. A 609, 1 (1996).
- [17] M. Sugita, Phys. Lett. B 394, 235 (1997).
- [18] Z. H. Wang, J. Xiang, W. H. Long, and Z. P. Li, J. Phys. G 42, 045108 (2015).
- [19] J. J. Sun, Z. Shi, X. Q. Li, H. Hua, C. Xu, Q. B. Chen, S. Q. Zhang, C. Y. Song, J. Meng, X. G. Wu, S. P. Hu, H. Q. Zhang, W. Y. Liang, F. R. Xu, Z. H. Li, G. S. Li, C. Y. He, Y. Zheng, Y. L. Ye, D. X. Jiang *et al.*, Phys. Lett. B 734, 308 (2014).
- [20] G. H. Bhat, W. A. Dar, J. A. Sheikh, and Y. Sun, Phys. Rev. C 89, 014328 (2014).
- [21] J. M. Yao, J. Meng, P. Ring, and D. Vretenar, Phys. Rev. C 81, 044311 (2010).
- [22] L. Guo, J. A. Maruhn, and P.-G. Reinhard, Phys. Rev. C 76, 034317 (2007).
- [23] A. D. Ayangeakaa, R. V. F. Janssens, C. Y. Wu, J. M. Allmond, J. L. Wood, S. Zhu, M. Albers, S. Almaraz-Calderon, B. Bucher, M. P. Carpenter, C. J. Chiara, D. Cline, H. L. Crawford, H. M. David, J. Harker, A. B. Hayes, C. R. Hoffman, B. P. Kay, K. Kolos, A. Korichi *et al.*, Phys. Lett. B 754, 254 (2016).
- [24] Y. Toh, C. J. Chiara, E. A. McCutchan, W. B. Walters, R. V. F. Janssens, M. P. Carpenter, S. Zhu, R. Broda, B.

- Fornal, B. P. Kay, F. G. Kondev, W. Królas, T. Lauritsen, C. J. Lister, T. Pawłat, D. Seweryniak, I. Stefanescu, N. J. Stone, J. Wrzesiński, K. Higashiyama *et al.*, Phys. Rev. C **87**, 041304(R) (2013)
- [25] A. Davydov and G. Filippov, Nucl. Phys. 8, 237 (1958).
- [26] A. M. Forney, W. B. Walters, C. J. Chiara, R. V. F. Janssens, A. D. Ayangeakaa, J. Sethi, J. Harker, M. Alcorta, M. P. Carpenter, G. Gürdal, C. R. Hoffman, B. P. Kay, F. G. Kondev, T. Lauritsen, C. J. Lister, E. A. McCutchan, A. M. Rogers, D. Seweryniak, I. Stefanescu, and S. Zhu, Phys. Rev. Lett. 120, 212501 (2018).
- [27] A. D. Ayangeakaa, R. V. F. Janssens, S. Zhu, D. Little, J. Henderson, C. Y. Wu, D. J. Hartley, M. Albers, K. Auranen, B. Bucher, M. P. Carpenter, P. Chowdhury, D. Cline, H. L. Crawford, P. Fallon, A. M. Forney, A. Gade, A. B. Hayes, F. G. Kondev, Krishichayan et al., Phys. Rev. Lett. 123, 102501 (2019)
- [28] S. Mukhopadhyay, B. P. Crider, B. A. Brown, S. F. Ashley, A. Chakraborty, A. Kumar, M. T. McEllistrem, E. E. Peters, F. M. Prados-Estévez, and S. W. Yates, Phys. Rev. C 95, 014327 (2017).
- [29] J. L. Wood, A.-M. Oros-Peusquens, R. Zaballa, J. M. Allmond, and W. D. Kulp, Phys. Rev. C 70, 024308 (2004).
- [30] S. Paschalis, I. Y. Lee, A. O. Macchiavelli, C. M. Campbell, M. Cromaz, S. Gros, J. Pavan, J. Qian, R. M. Clark, H. L. Crawford, D. Doering, P. Fallon, C. Lionberger, T. Loew, M. Petri, T. Stezelberger, S. Zimmermann, D. C. Radford, K. Lagergren, D. Weisshaar *et al.*, Nucl. Instrum. Methods Phys. Res. Sect. A 709, 44 (2013).
- [31] C. Y. Wu, D. Cline, A. Hayes, R. S. Flight, A. M. Melchionna, C. Zhou, I. Y. Lee, D. Swan, R. Fox, and J. T. Anderson, Nucl. Instrum. Methods Phys. Res. Sect. A 814, 6 (2016).
- [32] D. Cline, Bull. Am. Phys. Soc. 14, 726 (1969).
- [33] Y. Toh, T. Czosnyka, M. Oshima, T. Hayakawa, H. Kusakari, M. Sugawara, A. Osa, M. Koizumi, Y. Hatsukawa, J. Katakura, N. Shinohara, and M. Matsuda, J. Phys. G 27, 1475 (2001).
- [34] A. C. Rester, A. V. Ramayya, J. H. Hamilton, D. Krmpotic, and P. Venugopala Rao, Nucl. Phys. A **162**, 461 (1971).
- [35] D. C. Camp, Nucl. Phys. A **121**, 561 (1968).
- [36] R. Fournier, J. Kroon, T. H. Hsu, B. Hird, and G. C. Ball, Nucl. Phys. A 202, 1 (1973).
- [37] C. Morand, J. F. Bruandet, B. Chambon, A. Dauchy, D. Drain, A. Giorni, and T. U. Chan, Nucl. Phys. A 313, 45 (1979).
- [38] T. Czosnyka, D. Cline, and C. Y. Wu, Am. Phys. Soc 28, 745 (1983).
- [39] Gosia Manual, http://www.pas.rochester.edu/~cline/Gosia/ (2012), Accessed 05-29-2019.
- [40] J. M. Allmond, J. L. Wood, and W. D. Kulp, Phys. Rev. C 80, 021303(R) (2009).
- [41] B. Singh, Nucl. Data Sheets 74, 63 (1995).

- [42] T. Kibédi Jr., T. Burrows, M. Trzhaskovskaya, P. Davidson, and C. Nestor, Nucl. Instrum. Methods Phys. Res. Sect. A 589, 202 (2008).
- [43] R. Lecomte, M. Irshad, S. Landsberger, G. Kajrys, P. Paradis, and S. Monaro, Phys. Rev. C 22, 2420 (1980).
- [44] R. Lecomte, M. Irshad, S. Landsberger, P. Paradis, and S. Monaro, Phys. Rev. C 22, 1530 (1980).
- [45] H. Iwasaki, S. Michimasa, M. Niikura, M. Tamaki, N. Aoi, H. Sakurai, S. Shimoura, S. Takeuchi, S. Ota, M. Honma, T. K. Onishi, E. Takeshita, H. J. Ong, H. Baba, Z. Elekes, T. Fukuchi, Y. Ichikawa, M. Ishihara, N. Iwasa, S. Kanno *et al.*, Phys. Rev. C 78, 021304(R) (2008).
- [46] W. D. Kulp, J. M. Allmond, P. Hatcher, J. L. Wood, J. Loats, P. Schmelzenbach, C. J. Stapels, K. S. Krane, R.-M. Larimer, and E. B. Norman, Phys. Rev. C 73, 014308 (2006).
- [47] J. M. Allmond, R. Zaballa, A. M. Oros-Peusquens, W. D. Kulp, and J. L. Wood, Phys. Rev. C 78, 014302 (2008).
- [48] J. M. Allmond, J. L. Wood, and W. D. Kulp, Phys. Rev. C 81, 051305(R) (2010).
- [49] J. M. Allmond and J. L. Wood, Generalized triaxial rotor model (GTRM) code (unpublished) (2005).
- [50] J. M. Allmond and J. L. Wood, Coupled generalized triaxial rotor model (GTRM×2) code (unpublished) (2006).

- [51] J. Allmond and J. Wood, Phys. Lett. B 767, 226 (2017).
- [52] J. Meyer-Ter-Vehn, Nucl. Phys. A 249, 111 (1975).
- [53] K. Kumar, Phys. Rev. Lett. 28, 249 (1972).
- [54] D. Cline, Annu. Rev. Nucl. Part. Sci. 36, 683 (1986).
- [55] J. Srebrny, T. Czosnyka, C. Droste, S. Rohozinski, L. Prochniak, K. Zając, K. Pomorski, D. Cline, C. Wu, A. Backlin, L. Hasselgren, R. Diamond, D. Habs, H. Korner, F. Stephens, C. Baktash, and R. P. Kostecki, Nucl. Phys. A 766, 25 (2006).
- [56] A. Bohr and B. R. Mottelson, *Nuclear Structure* (World Scientific, Singapore, 1998), Vol. 2.
- [57] B. Brown and W. Rae, Nucl. Data Sheets 120, 115 (2014).
- [58] J. Henderson, Phys. Rev. C 102, 054306 (2020).
- [59] A. Poves, F. Nowacki, and Y. Alhassid, Phys. Rev. C 101, 054307 (2020).
- [60] S. Mukhopadhyay, B. P. Crider, B. A. Brown, A. Chakraborty, A. Kumar, M. T. McEllistrem, E. E. Peters, F. M. Prados-Estévez, and S. W. Yates, Phys. Rev. C 99, 014313 (2019).
- [61] J. Henderson, C. Y. Wu, J. Ash, B. A. Brown, P. C. Bender, R. Elder, B. Elman, A. Gade, M. Grinder, H. Iwasaki, B. Longfellow, T. Mijatović, D. Rhodes, M. Spieker, and D. Weisshaar, Phys. Rev. C 99, 054313 (2019).